The Astrophysical Journal, 988:282 (15pp), 2025 August 1 https://doi.org/10.3847/1538-4357/ade237

Detailed Time-resolved Spectral and Temporal Investigations of SGR J1550–5418 Bursts Detected with Fermi Gamma-Ray Burst Monitor

Mustafa Demirer[1], Ersin Göğüş[1], Yuki Kaneko[1], Özge Keskin[1], Sinem Şaşmaz[2], and Shotaro Yamasaki[3]

[1] Faculty of Engineering and Natural Sciences, Sabancı University, İstanbul 34956, Türkiye; mustafa.demirer@sabanciuniv.edu
[2] Department of Physics Engineering, İstanbul Technical University, İstanbul 34469, Türkiye
[3] Department of Physics, National Chung Hsing University, 145 Xingda Rd., South Dist., Taichung 40227, Taiwan

Received 2025 February 21; revised 2025 May 21; accepted 2025 June 4; published 2025 July 30

Abstract

We have conducted a time-resolved spectral analysis of magnetar bursts originating from SGR J1550−5418. Our analysis utilizes a two-step methodology for temporal segmentation of the data. We first generated and fitted overlapping time segments. Subsequently, we obtained nonoverlapping time segments with varying lengths based on their spectral evolution patterns, employing a machine learning algorithm called *k*-means clustering. For the fitting process, we employed three distinct models, namely a modified blackbody (MBB-RCS), a double blackbody (BB+BB), and a power law with an exponential cutoff (COMPT) model. We found that nearly all of the time segments fit well with the COMPT model. Both the average peak energy in the νF_ν spectra ($E_{\rm peak}$) and photon index parameters follow a Gaussian distribution with means ∼30 keV and −0.5, respectively. Furthermore, there is a strong positive correlation between the cooler and hotter temperature parameters of the BB+BB model, and both parameters show a Gaussian distribution with peaks ∼4 and 12 keV, respectively. Additionally, we found that the distribution of the temperature parameter of the MBB-RCS model can be fit with a skewed Gaussian function with a peak ∼9–10 keV. Lastly, we searched for quasiperiodic spectral oscillations (QPSOs) in the hardness ratio evolution of the bursts. We identified five potential QPSO candidates at frequencies ranging from ∼15 to ∼68 Hz. We discuss and compare these results with previous studies.

Unified Astronomy Thesaurus concepts: Neutron stars (1108); Magnetars (992); X-ray bursts (1814)

1. Introduction

Soft gamma repeaters (SGRs) are characterized by their emission of intense, short-duration bursts of hard X-rays and soft gamma rays, making them among the most luminous phenomena in these wave bands. These energetic events have attracted the high-energy astrophysics community since they were first discovered in the late 1970s (E. P. Mazets et al. 1979), being eventually revealed as a distinct class of events, different from any other galactic or extragalactic transient phenomena (J. L. Atteia et al. 1987; J. G. Laros et al. 1987).

SGRs are now prominent members of a small class of highly magnetized ($B \sim 10^{14}-10^{15}$ G; R. C. Duncan & C. Thompson 1992), isolated neutron stars, which are also known as magnetars. According to the magnetar framework (C. Thompson & R. C. Duncan 1995), extremely strong internal and external magnetic fields play a pivotal role in burst generation via reconnection or interchange instability in local settings of the neutron star crust. On rare occasions, magnetars also release much longer-duration giant flares releasing extraordinary amount of energies, reaching a level of 10^{45} erg (K. Hurley et al. 1999; D. M. Palmer et al. 2005).

SGR J1550−5418 was originally discovered with the Einstein X-ray satellite and received the designation 1E 1547.0−5408 (R. C. Lamb & T. H. Markert 1981). The source was identified as a magnetar with the detection of radio pulsations with the Parkes Radio Telescope at $P = 2.069$ s and a period derivative $\dot{P} = 2.318 \times 10^{-11}$ s s^{-1}, therefore yielding an inferred dipolar magnetic field strength 2.2×10^{14} G (F. Camilo et al. 2007).

The source did not exhibit any X-ray bursts until 2008, at which point a significant change occurred in its behavior, entering a series of three burst-active episodes. The first episode commenced in 2008 October with several tens of bursts (A. von Kienlin et al. 2012). The second episode started on 2009 January 22 and became the most burst-active phase of the source to date, emitting hundreds of bursts (A. J. van der Horst et al. 2012). This episode of activity started with a cluster of bursts with enhanced underlying emission in soft gamma rays, as detected with the Gamma-ray Burst Monitor (GBM) on the Fermi Gamma-ray Space Telescope (Fermi; Y. Kaneko et al. 2010), and also emitted highly energetic bursts with pulsating tails (S. Mereghetti et al. 2009). The third burst-active episode of SGR J1550−5418 was in 2009 March–April (A. J. van der Horst et al. 2012).

Numerous detailed studies have been performed to reveal the spectral properties of short bursts from various magnetars, utilizing both thermal and nonthermal models (see, e.g., M. Feroci et al. 2004; G. L. Israel et al. 2008; A. C. Collazzi et al. 2015). Particularly for the bursts of SGR J1550−5418, L. Lin et al. (2012), A. J. van der Horst et al. (2012), and D. Kırmızıbayrak et al. (2017) conducted time-integrated spectral investigations in various energy ranges. These extensive studies revealed that either a combination of thermal models using two blackbody functions (BB+BB) or a power law with an exponential cutoff (COMPT) function successfully described the spectra of most bursts. The COMPT model posits that photons originating from the ignition region undergo successive Compton upscatterings in the magnetosphere by electron–positron pairs (L. Lin et al. 2011). For this model, A. J. van der Horst et al. (2012) determined an average power-law photon index −0.92, and an average peak energy in the νF_ν spectra ($E_{\rm peak}$) ∼40 keV from time-integrated spectral analysis of 286 bursts of SGR J1550−5418. On the other hand, the BB+BB model proposes the existence of a compact, hotter inner region in the magnetosphere, nested within a larger, colder outer region. This type of structure arises from energy dissipation in the outer regions. Previous time-integrated spectral studies revealed blackbody temperatures of 2–4 keV in the cooler region and 10–15 keV for the hotter emitting region (M. Feroci et al. 2004; L. Lin et al. 2012; A. J. van der Horst et al. 2012; D. Kırmızıbayrak et al. 2017).

Subsequently, G. Younes et al. (2014) performed a detailed time-resolved spectral investigation of bright bursts from SGR J1550−5418. In particular, their primary aim was to address the issue of the brightest time intervals dominating the overall time-integrated burst analysis and achieve a more comprehensive understanding of burst dynamics and spectral properties, by employing BB+BB and COMPT models. In their COMPT model analysis, a negative correlation between the burst flux and $E_{\rm peak}$ is observed up to a flux limit of $F \approx 10^{-5}\,{\rm erg\,s^{-1}\,cm^{-2}}$, beyond which the correlation becomes positive. On the other hand, using the result of the BB+BB model fits, they found that the area of the emission region versus temperature follows a broken power law of negative trend: For bursts with low flux, the same negative trend is seen across the temperatures, while as the burst flux increases a power-law break emerges, which may be attributed to adiabatic cooling (G. Younes et al. 2014). However, their spectral extraction from particular time intervals was done based on a set criterion; in other words, each successive spectrum was accumulated until a certain signal-to-noise ratio was achieved. Although this is a common practice in time-resolved spectral analysis to ensure sufficient statistics, this method of binning could possibly prevent us from seeing the real spectral evolution within the burst, which in turn may hinder real insight into the spectral properties of magnetars.

In addition to these spectral properties that allow us to probe the emission mechanism of magnetar bursts, observations of quasiperiodic oscillations (QPOs) in the light curves of two galactic giant flares stand out as particularly remarkable features regarding the interiors of magnetars (G. L. Israel et al. 2005; T. E. Strohmayer & A. L. Watts 2005, 2006). It was already predicted by R. C. Duncan (1998) that the solid crust of a magnetar and its high-magnetic-field coupling may result in large-scale magnetic reconfigurations that have the potential to rupture the crust. The X-ray and gamma-ray flux oscillations manifesting as QPOs could be the result of global seismic vibrations caused by such occurrences. However, due to the very short durations of typical magnetar bursts, identifying QPO features in them is more challenging.

For SGR J1550−5418, D. Huppenkothen et al. (2014) analyzed 263 short bursts from its 2009 burst storm. By employing a Bayesian method, they identified two QPOs at ∼93 Hz, one at 127 Hz, and a broad signal at 260 Hz. They also showed that these frequencies, consistent with those observed in giant flares, are likely linked to global magnetoelastic oscillations (D. Huppenkothen et al. 2014). Recently, X. Li et al. (2022) investigated a burst from another prolific bursting magnetar, SGR J1935+2154, associated with the fast radio burst FRB 200428 (C. D. Bochenek et al. 2020). They identified a significant QPO signal at ∼40 Hz, which marks one of the strongest (3.4σ) QPO detections in nongiant flare bursts. Similarly, S. Xiao et al. (2024) conducted an analysis of QPOs and power density spectra (PDS) from bursts of the SGR J1935+2154. Their study focused on both individual bursts and averaged PDS to identify potential QPO signals. Although no significant QPO detections above 3σ were found, the study revealed ∼40 Hz candidates in several bursts, consistent with prior findings in the burst associated with FRB 200428. The detected (or candidate) QPOs described above were revealed using time-series data, however O. J. Roberts et al. (2023) recently extended this framework to search for quasiperiodic variations in the spectra of magnetar bursts. In particular, they reported the first detection of quasiperiodic spectral oscillations (QPSOs) in the $E_{\rm peak}$ parameter of X-ray bursts from SGR J1935+2154, at ∼42 Hz. They proposed that these spectral oscillations likely originate from acoustic waves traveling through a magnetized flux tube, which works as an acoustic cavity. From the observational point of view, it is not known how rare these intriguing cases are as no systematic search for such oscillations in bright magnetar bursts has been performed.

The spectral analysis part of our study was constructed upon the method introduced by Ö. Keskin et al. (2024), which investigated the spectral evolution of bursts from SGR J1935+2154 using a novel two-step approach briefly described below.[4] Clustering-based time-resolved X-ray spectra were fit using the three models COMPT, BB+BB, and a physically motivated modified blackbody with resonant cyclotron scattering (MBB-RCS). They demonstrated that the COMPT model was preferred for most spectra and revealed correlations between spectral parameters and flux. In this paper, we present the clustering-based time-resolved spectral analysis of 44 bright bursts from SGR J1550−5418. In particular, instead of generating spectra with uniform time segments or those based on signal-to-noise ratio, we generated spectra for overlapping time segments which were subsequently analyzed as the first phase. Furthermore, to grasp the spectral change points in the bursts, we employed machine-learning-based clustering algorithms to create time segments of varying lengths based on the spectral parameters obtained in the first phase. This innovative technique allowed us to gain deeper insights into the burst properties under investigation. In addition, we present the results of our systematic QPSO search with SGR J1550−5418 bursts, where we found five QPSO burst candidates. This paper is organized as follows. We introduce the instrument, burst data, and data selection in Section 2. The spectral analysis methods and their results are presented in Section 3. The search for QPSOs and their results are delivered in Section 4. We discuss both our spectral and timing results in Section 5.

2. Observations and Data Selection

The data used in this study were collected with Fermi, which consists of two primary instruments: the Large Area Telescope (LAT) and the GBM. The LAT is capable of detecting gamma rays with energies in the ∼20 MeV–∼300 GeV range. The GBM has the capability of observing lower-energy photons, ranging from ∼8 keV to ∼40 MeV. It consists of 12 thallium-activated sodium iodide (NaI) scintillation detectors and two bismuth germanate (BGO) scintillation detectors with energy ranges from ∼8 keV to ∼1 MeV and ∼200 keV to ∼40 MeV, respectively (see W. B. Atwood et al. 2009; C. Meegan et al. 2009 for further information about the telescope and detectors). We employed the GBM NaI detectors for our

---

[4] See Ö. Keskin et al. (2024) for details of the methodology.

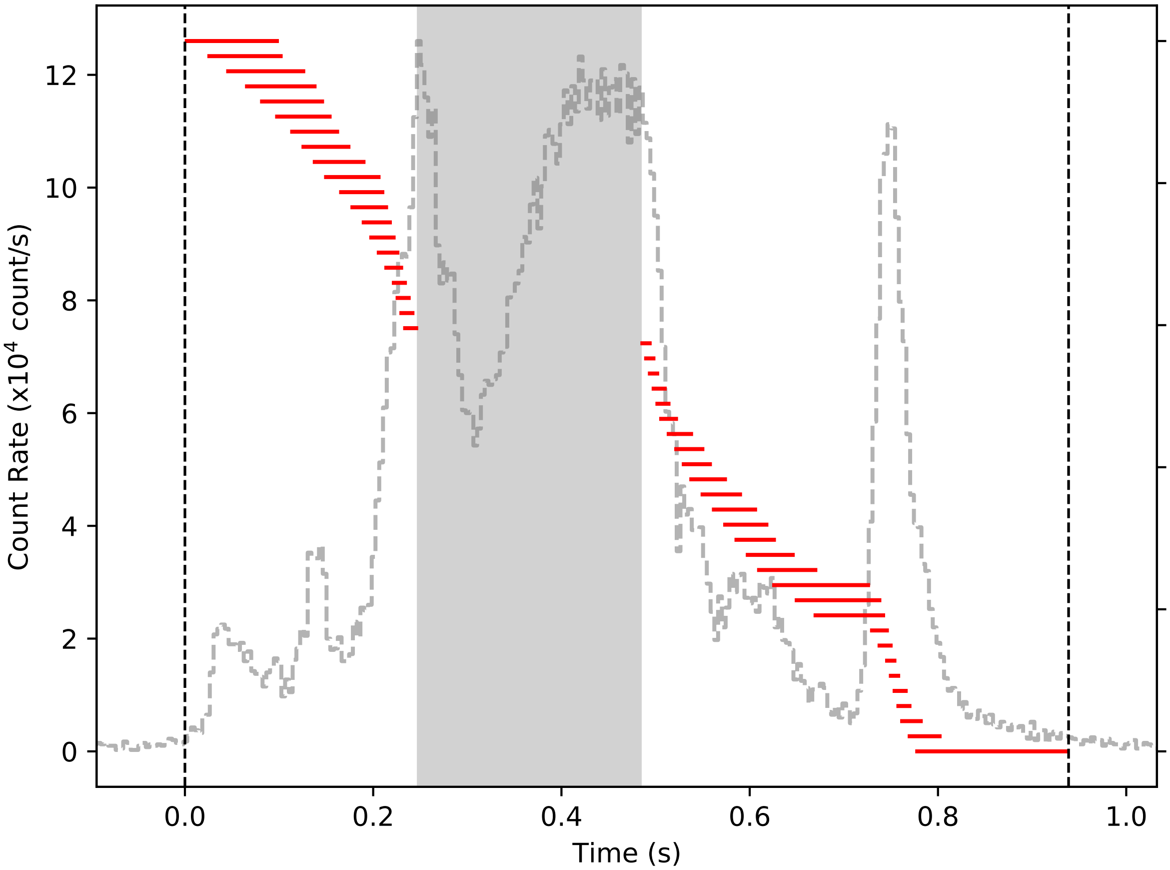

Figure 1. Light curve of an SGR J1550−5418 burst observed on 2009 January 22 at 06:49:48.321 UTC, shown for the brightest detector (n2). Vertical dashed lines indicate the start and end times of the Bayesian block duration. The red horizontal lines represent 48 overlapping time segments, with each consecutive segment overlapping by 80%. The gray portion corresponds to the saturated part of the burst, and spectral analysis is not applied in this range. We note that the red lines are intended to display the time span of each segment with an arbitrary *y*-scale.

analyses, as the majority of emission from typical magnetar bursts occurs below ∼200 keV (L. Lin et al. 2012; A. J. van der Horst et al. 2012; G. Younes et al. 2014). Among the three data types provided by the GBM, we utilized Time-Tagged Event data due to their superior temporal (2 μs) and energy (128 channels) resolution.

We compiled our burst sample from the magnetar burst catalog of A. C. Collazzi et al. (2015), which includes 386 bursts from SGR J1550−5418 during its 2008–2009 active episodes. We selected bright bursts with a background-subtracted count above the threshold of 1200 counts (see Ö. Keskin et al. 2024 for the reasoning behind this threshold) in the brightest detector to ensure that the results of our spectral analysis are statistically significant. As a result, we obtained a total of 74 bursts that suit our criterion, listed in Table A1 in the Appendix. Among these events, 30 were saturated; that is, the brightest portion of the burst exceeded the limits of the GBM data readout capability of 375,000 counts s^{-1} for all detectors (C. Meegan et al. 2009). The energy spectra accumulated during these saturated time intervals could suffer from the pulse pileup effect and may not represent correct energy distribution. Therefore, we excluded the saturated parts of these 30 bursts from our study and subjected only the remaining unsaturated parts to the analysis (see Figure 1 for an example). Our analysis was performed in the energy range 8–200 keV, employing 4 ms minimum time resolution, consistent with Ö. Keskin et al. (2024). In addition, we excluded the energy range between 30 and 40 keV for the spectral fit statistics calculations to prevent interference from the iodine K-edge.[5] Nevertheless, we also performed fits with this energy band included, compared the two results (i.e., 30−40 keV included and excluded), and confirmed that the exclusion does not significantly affect the parameters or their uncertainties.

We used the data collected with three detectors for which the detector zenith-to-source angles are the smallest and less than 60° for each burst. In some cases, only two detectors satisfied this angle criterion. Additionally, we excluded detectors whose fields of view were either partially or fully blocked by the spacecraft itself from our analysis.[6]

3. Time-resolved Spectral Analysis

For the time-resolved spectral analysis, instead of conventional time binning based on the observed signal strength, we applied the method introduced in Ö. Keskin et al. (2024), a clustering-based binning approach that identifies significant change points in spectral behavior within the burst. Accordingly, our analysis was done in two phases: (i) overlapping time-resolved spectral analysis, and (ii) clustered time-resolved spectral analysis. To this end, we first segmented our bursts into overlapping time segments within duration intervals that were calculated using a Bayesian blocks representation of the burst light curves (J. D. Scargle et al. 2013). The burst duration was calculated

---

[5] https://fermi.gsfc.nasa.gov/ssc/data/analysis/GBM_caveats.html

[6] We checked the blockage using the GBMBLOCK software provided by the GBM team.

based on data from the brightest NaI detector, with background levels estimated from Bayesian blocks longer than 4 s. Blocks above this background level were considered burst intervals, and the duration was taken as the time from the first to the last burst block (see Appendix A of Ö. Keskin et al. 2024 for details). Through this overlapping segmentation, our objective was to capture the spectral evolution with as much detail as possible while still keeping sufficient statistics.

We created the first time segment with a time length that encompasses 1200 burst background-subtracted counts (in the brightest detector). The next time segment began from one-fifth of the duration of the first time segment and continued until the threshold count of 1200 was accumulated. In doing so, we acquired 80% overlapping time segments (see Figure 1). As a result, we obtained a total of 522 overlapping time segments from 74 bursts, listed in Table A1 in the Appendix, for which spectra in the 8–200 keV were extracted.

3.1. Spectral Analysis and Model Comparison

For the spectral analysis performed in this study, we used the X-ray Spectral Fitting Package (XSPEC, version 12.12.1). We generated detector response matrices for each detector for all untriggered events in our sample with the GBM Response Generator, released by the Fermi-GBM team. We employed three different spectral models; a modified blackbody with resonant cyclotron scattering (MBB-RCS; Y. E. Lyubarsky 2002; S. Yamasaki et al. 2020),[7] a sum of two blackbodies (BB+BB),[8] and a power law with an exponential cutoff (COMPT).[9] The BB+BB and COMPT models are commonly used in magnetar burst analyses, as discussed in Section 1. The MBB-RCS model, on the other hand, is physically motivated considering thermal emission—specifically, blackbody radiation modified (MBB; M. Lyutikov 2003) by radiative transfer through the trapped fireball interior. This outgoing radiation then undergoes further resonant cyclotron scattering (RCS; S. Yamasaki et al. 2020) by magnetospheric particles during magnetar bursts. This model successfully explains typical intermediate bursts from SGR J1935+2154 by adjusting the effective blackbody temperature $T_{\rm eff}$ of the MBB radiation (S. Yamasaki et al. 2020). All spectral fits were performed by minimizing the Castor statistics (C-stat; W. Cash 1979). The C-stat we obtain from a fit is based on the maximum likelihood, and it alone does not provide a measure to test the goodness of fit. Therefore, we utilized the method suggested by J. S. Kaastra (2017) to calculate the variance and expected value of the C-stat. In turn, we determined acceptable C-stat values (at 3σ level) for each photon model of each spectrum. Even though the goodness calculation provides information on the statistical acceptability for each photon model fitting, it does not yield information for comparing different fits with one another. Therefore, we also used the Bayesian information criterion (BIC; G. Schwarz 1978) as a model preference metric:

$$\mathrm{BIC} = -2\ln\mathcal{L}_{\max} + m\ln N = \text{C-stat} + m\ln N.$$

Here, $\mathcal{L}_{\max}$ is the maximum likelihood, m represents the number of parameters in the spectral model, and N describes the number of data points. We compared the difference in BIC values (ΔBIC) for the pairs of continuum model fits (BB+BB versus COMPT, COMPT versus MBB-RCS, and BB+BB versus MBB-RCS). In the comparison of the two models, when the ΔBIC was greater than 10 (corresponding to a Bayes factor of ~150, implying a likelihood ratio confidence level greater than 99%; R. E. Kass & A. E. Raftery 1995), we adopted the model with a lower BIC value as the preferred choice. However, in cases where the BIC difference was less than 10, we accepted both models as favorable due to their comparable goodness of fit given that the fit parameters were well constrained.

After fitting all overlapping time-segment spectra with the three models and obtaining their BIC values, we found that 495 spectra (i.e., ~95% of the sample) can be modeled well with the COMPT model; that is, the COMPT model fits are either the most preferred based on ΔBIC or have comparable BIC values as those of the alternative models. The other two, the BB+BB and MBB-RCS models, are less preferred and perform similarly, the former model being preferred for 69% of the spectra, while the latter preferred for 58% of them.

Following the first round of fitting (that is, modeling the spectra of overlapping time segments), we clustered these overlapping time segments in order to form nonoverlapping time segments determined by significant changes in spectral properties. For this process, we implemented a machine learning algorithm called k-means clustering (J. B. MacQueen 1967) from the `scikit-learn` Python library (F. Pedregosa et al. 2011) to identify significant spectral change points in each of the bursts. The k-means algorithm partitions data into k clusters by minimizing intra-cluster variance. Since the COMPT model was preferred for most of the spectra, we employed both the $E_{\rm peak}$ and photon index parameters of the COMPT model along with the midpoint of each time segment as features for the clustering algorithm with appropriate scaling. The algorithm requires the number of clusters (k) to be specified at initialization. To determine the optimal number of clusters, we developed a method based on the inertia versus k graph, using the average inertia of the highest 25% of k values plus a small offset. The reciprocal of $E_{\rm peak}$ and photon index errors was used as a weight in the inertia calculation to account for parameter uncertainties. A detailed description of the k-means clustering implementation used in this study can be found in the Appendix of Ö. Keskin et al. (2024).

In Figure 2, we present an example of clusters obtained with the k-means algorithm for one of the bursts in our sample. As seen in the figure, the time segments that fall between two adjacent clusters identified by the algorithm remain overlapped, and the exact beginning and end times of each cluster need to be systematically determined. To address this issue, we halved the background-subtracted counts in the overlapping regions of the consecutive clusters, and assigned half of the counts to the preceding time segment and the other half to the next time segment. We note that we did not apply the k-means algorithm to 16 of the bursts in our sample that provided less than three overlapping time segments, which is an insufficient number for clustering. In addition, after applying the k-means algorithm to the remaining bursts, we find 14 bursts yielding a single cluster each. Hence, these 14 events were excluded from further analysis since it was no longer possible to perform time-resolved analysis on these bursts.

---

[7] Implemented in XSPEC using an additive table model component (atable). The table is available at doi:10.5281/zenodo.10485159.

[8] Implemented in XSPEC as bbody + bbody.

[9] Implemented in XSPEC as a user-defined function: $f(E) = A\exp[-E(2+\Gamma)/E_{\rm peak}](E/50\,\mathrm{keV})^{\Gamma}$.

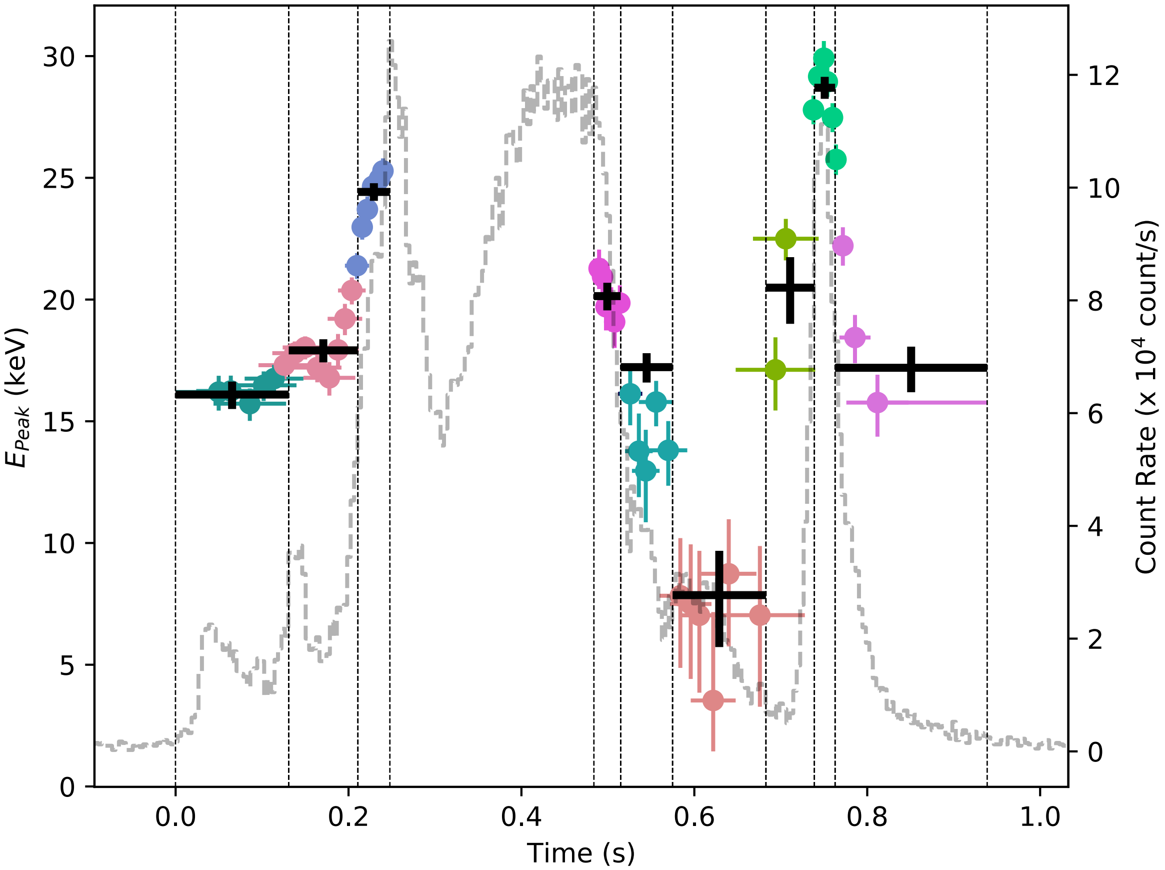

Figure 2. $E_{\rm peak}$ values for 48 overlapping time segments (filled circles with 1σ uncertainties) for the same burst shown in Figure 1. The light curve is shown with gray dashed lines (right axis). The data points were colored by nine spectrally distinctive clusters determined via k-means clustering, the intervals of which are shown with vertical dotted lines. Black crosses show the $E_{\rm peak}$ values with 1σ uncertainties obtained from the COMPT fits to the nine cluster segments in the second stage of spectral analysis.

After clustering and the above-mentioned exclusion, we obtained nonoverlapping time segments ranging from two to nine per burst, with an average of three time segments per burst. We then refit these 151 nonoverlapping time segments using our three spectral models. We found that approximately ∼93% of them can be fit with the COMPT model, while approximately ∼53% of them can be fit with the BB+BB model and ∼55% with the MBB-RCS model. Note that some time segments are well fit by multiple models. These results are broadly consistent with the findings from overlapping time segments.

3.2. Clustering-based Spectral Analysis Results

Since the COMPT model fits the majority of our spectra, we first discuss the parameters of this model. Note that all uncertainties presented here are at the 1σ level. We present a scatter plot of the photon index and $E_{\rm peak}$ values of the COMPT model in Figure 3 along with the distributions, all color-coded by the energy flux. We find that the photon indices (Γ), which range from –2 to 1, are distributed as a Gaussian (Figure 3(b)) with a mean value -0.57 ± 0.04 and a width 0.43 ± 0.04 (reduced chi-square, $\chi^2_\nu = 0.83$). The distribution of $E_{\rm peak}$ also follows a Gaussian (see Figure 3(c)) whose mean is at 30.65 ± 0.95 keV and width 8.46 ± 0.98 keV ($\chi^2_\nu = 0.86$). The energy flux of these spectra in the 8−200 keV band ranges from 1×10^{-6} to 9.82×10^{-5} erg cm^{-2} s^{-1}, while the energy fluence values are between 1.9×10^{-7} and 1.6×10^{-6} erg cm^{-2}.

We find no correlation between the parameters of the COMPT model (i.e., $E_{\rm peak}$ and Γ). On the other hand, we find a positive correlation between the index and the corresponding flux (Spearman's rank-order correlation coefficient $\rho = 0.62$, and the chance probability of such correlation to occur from a random data set $p = 9.8 \times 10^{-18}$). As seen in Figure 3, the spectra with the highest flux yield photon indices around 0.5 and $E_{\rm peak}$ tightly clustered near 40 keV. Meanwhile, the $E_{\rm peak}$ of the spectra at lower flux levels span nearly the same range from about 15 to 45 keV.

Regarding the thermal models, we present a scatter plot of the two kT values of the BB+BB model in Figure 4 along with the distributions, again color-coded by the energy flux. We find that the cooler component (kT_l) of the BB+BB model exhibits a Gaussian distribution which peaks at 4.64 ± 0.07 keV with a width of 0.72 ± 0.07 ($\chi^2_\nu = 0.83$), and is characterized by a narrow spread between 2 and 7 keV (Figure 4(c)). However, the hotter component (kT_h) of the same model exhibits a much broader distribution, spanning from 6 to 20 keV, and its Gaussian fit curve value has a peak at 13.16 ± 0.22 keV and a width of 2.93 ± 0.26 ($\chi^2_\nu = 0.90$; Figure 4(b)). We observe a statistically significant positive correlation between the parameters kT_l and kT_h, with $\rho = 0.59$ and a p-value of 1.3×10^{-11}. Additionally, we find a moderate but significant positive correlation between kT_l and the energy flux ($\rho = 0.41$, $p = 1.1 \times 10^{-5}$), suggesting that higher flux levels are typically associated with higher values of kT_l. Conversely, kT_h does not exhibit any significant correlation

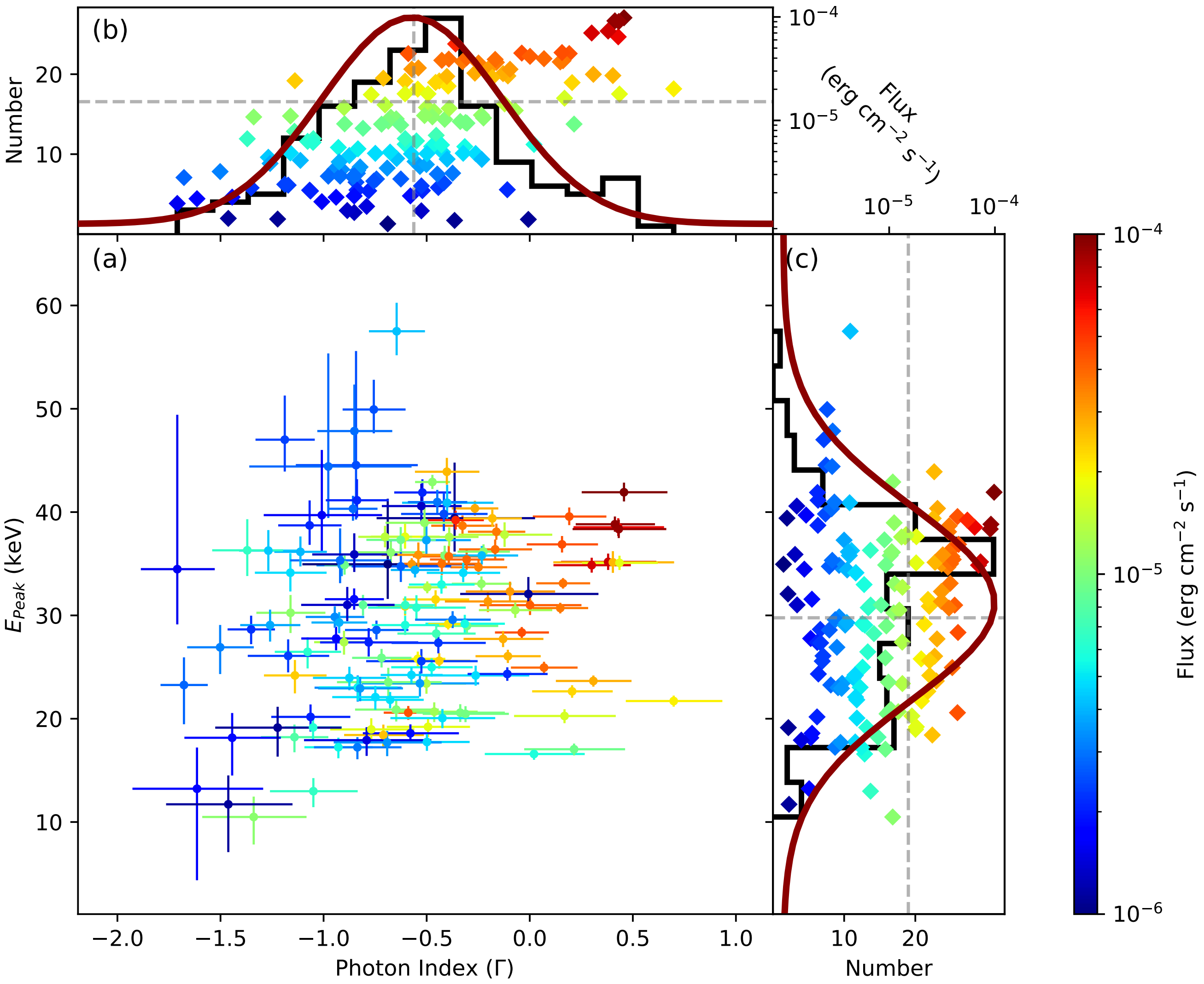

Figure 3. (a) Scatter plot of $E_{\rm peak}$ vs. photon index of the COMPT model fits for 141 spectra. Corresponding energy flux values are color-coded. (b) Distribution of photon index values. The best-fit Gaussian function model is shown in brown, and corresponding flux values are shown as diamond data points. The gray dashed line shows the mean value of the fluxes. (c) Distribution of $E_{\rm peak}$. The best-fit Gaussian function model is shown in brown, and corresponding flux values are shown as diamond data points. The gray dashed line shows the mean value of the fluxes.

with the energy flux. For intermediate flux levels, kT_l values are mostly confined to the range of 3–6 keV. In contrast, kT_h values span nearly the entire range from 7.5 to ∼20 keV across all flux levels except for the highest-flux segments, where kT_h is located in a narrower range between 10 and 11 keV.

Finally, the MBB-RCS model temperatures (kT_m) are presented in Figure 5. The distribution of kT_m is between the kT_l and kT_h values of the BB+BB model, as expected, ranging from 4 to 11 keV (Figure 5(a)). Even though the sample size is limited, the distribution of kT_m values is more complex than a Gaussian-like distribution, being consistent with a skewed Gaussian distribution. The skewed Gaussian fit has a mean value of 10.20 ± 0.18 and a width of 3.89 ± 0.65 ($\chi^2_\nu = 0.70$). Regarding the flux dependence of the MBB-RCS model, the lower and middle flux values are distributed over all kT_m values. However, the highest flux values are accumulated around the 8–11 keV region.

4. Search for Quasiperiodic Spectral Oscillations

In addition to spectral investigation, we extended our analysis to explore for any presence of QPOs in the bursts of SGR J1550−5418. In this effort, we were motivated by the findings of O. J. Roberts et al. (2023), which report possible QPSO signatures in SGR J1935+2154. SGR J1550−5418 is another such prolific magnetar and numerous of its bursts are bright enough and well suited for such a search. However, the SGR J1550−5418 bursts in our sample consist of very few time segments. Therefore, it was not possible to utilize the $E_{\rm peak}$ parameter to search for potential QPSOs. In order to extend the systematic search for QPSOs in a larger burst sample, we performed temporal search using the hardness ratio (HR) instead. This can be justified given the fact that the photon index parameter remains nearly constant during all of the bursts. (HR variations closely follow the time evolution in $E_{\rm peak}$.) Moreover, we diagnosed the use of HRs rather than spectral parameters (namely $E_{\rm peak}$) for searching QPSOs using GBM data of SGR J1935+2154 bursts, which show a prominent QPSO as reported by O. J. Roberts et al. (2023). We find the HR oscillations at around 45 Hz to be consistent with the reported value, with a chance occurrence probability of 0.0068.

For HR evolution, we first obtained a light curve with 4 ms time resolution for each burst by combining the data collected

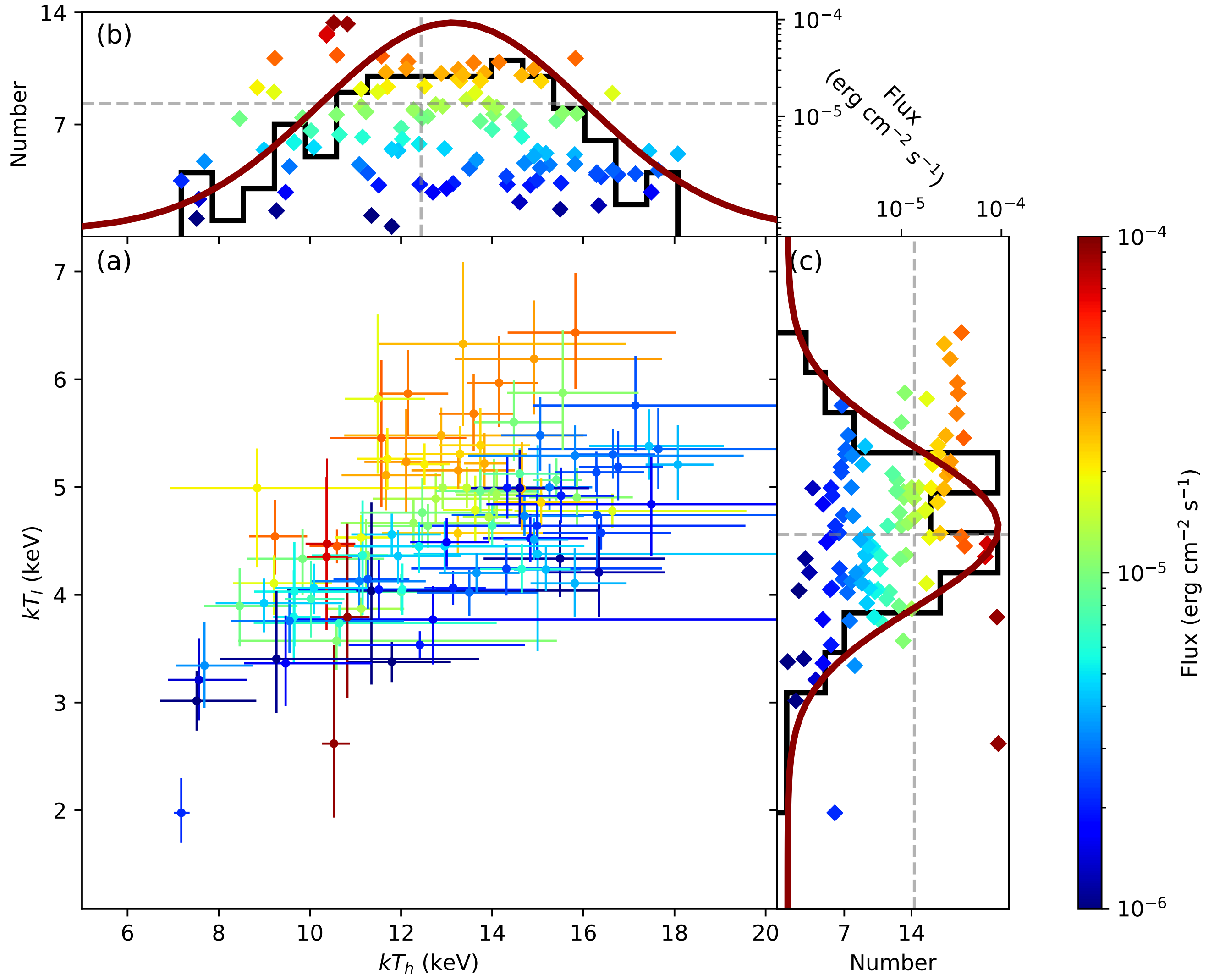

Figure 4. (a) Scatter plot of kT_l vs. kT_h parameters that can be described with BB+BB (80 spectra). Corresponding flux values are color-coded. (b) Distribution of kT_h. The best-fit Gaussian function model is shown in red, and corresponding flux values are shown as diamond data points. The gray dashed line shows the mean value of the fluxes. (c) Distribution of kT_l values. The best-fit Gaussian function model is shown in red, and corresponding flux values are shown as diamond data points. The gray dashed line shows the mean value of the fluxes.

with the detectors included in the spectral analysis. We then calculated HRs in the 8–200 keV energy range with varying energy pivots ($E_{\rm piv}$) between 10 and 50 keV, where $E_{\rm piv}$ represents the energy threshold separating the soft and hard energy bands. We defined the HR as the ratio of background-subtracted counts in two different energy bands: $E_{\rm piv} - 200$ keV and $8 - E_{\rm piv}$. In order to avoid negative background-subtracted counts of the light curve and to obtain statistically reliable HR evolution throughout each burst, we required that a given HR must be constrained within at least a 3σ level ($\geqslant 3$ times of its own error). Therefore, if the background-subtracted counts in a 4 ms time bin do not satisfy this criterion, we added the counts of the next time bin until a reliable HR was obtained.

In the QPSO search process, we first eliminated the underlying long-term variations in the HR curve by fitting a third-degree polynomial to the HR data and analyzed the residuals. We then employed two different methods for our analysis: the Lomb–Scargle periodogram (LSP; N. R. Lomb 1976; J. D. Scargle 1982) and weighted wavelet z-transform (WWZ; G. Foster 1996). The LSP was chosen because it is a well-suited tool for time-series analysis of unevenly sampled data sets. However, since the LSP does not account for temporal variations, we complemented it with the WWZ, which provides time-resolved spectral analysis. For the WWZ method, we employed a Fortran code as provided by G. Foster (1996), and for the LSP method we utilized the Astropy package (Astropy Collaboration et al. 2022).

The frequency range used in both methods was obtained as follows. The minimum frequency was set to 10 Hz, based on the durations of typical magnetar bursts (~0.1 s). The maximum search frequency was obtained by taking the minimum spacing of HR steps (i.e., $\Delta t = 2$ ms) into account, as $1/(2\Delta t) = 250$ Hz. This is analogous to the Nyquist frequency in searches of evenly sampled time-series data.

In the LSP, we used 20 samples per peak corresponding to a frequency resolution of 0.1 Hz, and quantified the significance of detected peaks using the false-alarm probability calculated using the method of R. V. Baluev (2008). For the WWZ method, we adopted the same frequency resolution. We tested various Gaussian window sizes (c) to examine their impact on the QPSO results but found no noticeable differences. Therefore, we selected $c = 0.005$, as this value is an order of magnitude smaller than the shortest QPSO candidate

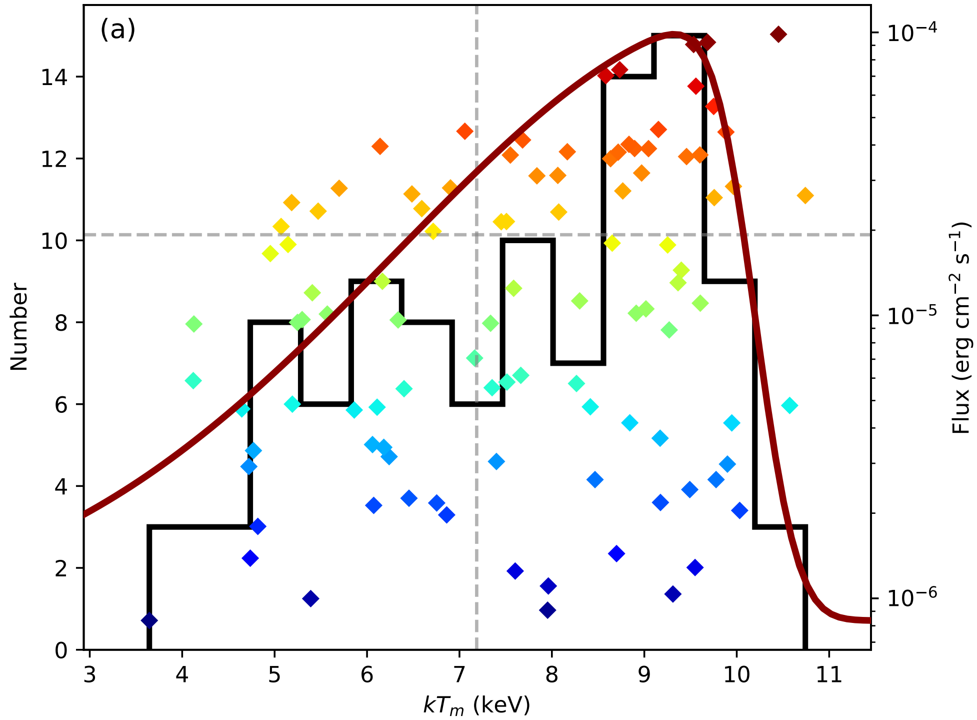

Figure 5. Time-segment distribution of the MBB-RCS model temperature, kT_m, for 83 spectra. The flux values of each individual time segment are shown in logarithmic scale and color-coded diamond data points. The best skewed Gaussian fit is drawn in red. The gray dashed lines show the mean value of the fluxes and kT_m parameter, respectively.

duration. In addition, we utilized F-statistics values to determine QPSO significance.

For the WWZ method, we first searched the entire burst interval. We identified the time interval(s) in the wavelet periodograms corresponding to a p-value of less than approximately 0.1, and further narrowed down the precise search interval of the QPSO candidate using both methods (see color plot in Figure 6).

The procedure described above was repeated for all bursts and across multiple pivot point energies ranging from 15 to 30 keV in 1 keV increments. We systematically examined each burst with all $E_{\rm piv}$ values and identified five bursts with QPSO candidates ranging from 15.2 to 67.84 Hz, each detected at a specific fixed $E_{\rm piv}$ value. The candidate signals in the resulting power spectra were fit with a Lorentzian function to determine their peak frequency values, and the full width at half-maximum (FWHM). Additionally, coherence values (Q = peak frequency/FWHM) were calculated to assess the broadness of the peaks. All resulting Q values exceed 2, which is the conventional threshold to label a feature as a QPO (M. van der Klis 2006). These results along with p-values (chance probability) are tabulated in Table 1.

The most significant QPSO candidate is in burst MET 254366383.448 (hereafter QPSOa; Figure 6, top panel). The search yields a pivot energy of 29 keV, and exhibits oscillations at 29.0 Hz with a FWHM of 7.1 Hz (using WWZ) and 27.9 Hz with a FWHM of 10.9 Hz (using LSP). The corresponding p-values of these detections are 0.0568 and 0.0066, respectively. The QPSO spans the entire burst duration of 0.12 s. The spectral analysis reveals that the burst comprises three nonoverlapping time segments, with $E_{\rm peak}$ values ranging from about 35 to 30 keV.

The second QPSO candidate, in burst MET 254299756.841 (QPSOb; Figure 6, bottom panel), originates from the brightest unsaturated burst. This burst consists of nine nonoverlapping spectral segments and the QPSO candidate spans the burst from the beginning until the end, excluding the last segment, which primarily consists of the dimmer, low-energy tail of the burst. Although we initially applied the same procedure described above to search for QPSO candidates in this burst, we detected an oscillation peak at a frequency of approximately 15 Hz, corresponding to a region dominated by red noise (D. Huppenkothen et al. 2013). Thus, our previously utilized significance estimation methods (e.g., Baluev's method), which assume Gaussian white noise, are not suitable in this scenario. As an alternative, we calculated the wavelet transform and its associated significance level using the algorithm by C. Torrence & G. P. Compo (1998), which is specifically designed to accommodate red-noise assumptions. This approach is uniquely applicable to this particular burst due to its highly regular sampling, namely 91.11% of time intervals matched the minimal unbinned sampling interval of 0.002 s. Using this wavelet method, we identified oscillations with a frequency of 15.73 Hz and a corresponding FWHM of 2.67 Hz. The calculated p-value for this detection is 0.0001, which corresponds to a significance of $\sim 3.67\sigma$. Although we could not compute a similar significance level for the LSP method due to red-noise limitations, the QPSO candidate from the LSP analysis exhibits distinct harmonic-like structures around 30 and 120 Hz. It is important to note that this burst stands out from other QPSO candidates in two notable ways: it exhibits a significantly lower peak frequency, and has the longest duration of 0.29 s. Moreover, being the brightest unsaturated burst analyzed, it unsurprisingly displays the highest Q value of 5.89 measured in the wavelet method. Additionally, its $E_{\rm peak}$ values drop from about 20 keV at the start to 13 keV at the end of the QPSO, and are considerably lower than those of other candidates, which typically range from 30 to 40 keV.

The QPSO candidate in burst MET 254291434.732 (QPSOc) is another persistent QPSO spanning the entire burst duration. This burst is relatively short, with a duration of

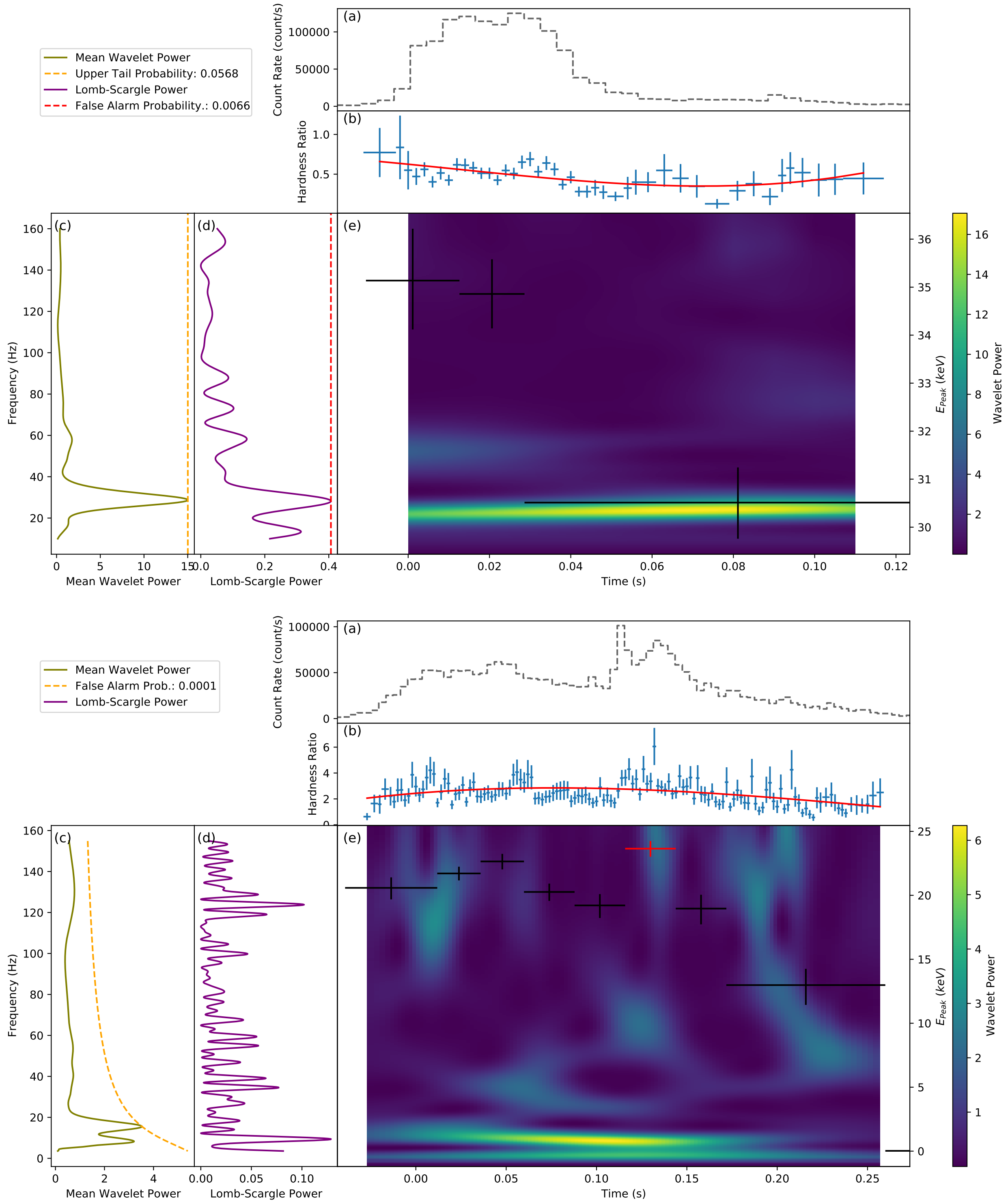

Figure 6. Top panel: combined plot of the most significant candidate, QPSOa (MET: 254366383.448). Bottom panel: combined plot of candidate QPSOb (MET: 254299756.841). In both figures (a) the light curve, (b) the hardness ratio vs. time, fit with a third-degree polynomial, (c) the time-averaged WWZ plot, and (d) the Lomb–Scargle periodogram as a function of frequency are shown. In panels (c) and (d), the maximum values are indicated by dashed lines, with their corresponding *p*-values provided in the legend. Please note that a *p*-value cannot be calculated using the LSP method for QPSOb. Panel (e) gives the WWZ contour plot with time and frequency axes, where power is color-coded. Overlaid on panel (e) are the $E_{\rm peak}$ values for each time segment derived from the spectral analysis. All time segments, except for the sixth time segment of QPSOb (highlighted in red), are best described by the COMPT model based on BIC comparisons. Although the analysis spans the 10–250 Hz frequency range, the plots are limited to 160 Hz for clarity.

0.15 s, and consists of only one nonoverlapping time segment with an $E_{\rm peak}$ of 40.3 keV. The QPSO candidate exhibits oscillation frequencies of 27.8 Hz (WWZ) and 29.5 Hz (LSP), with FWHM values of 8.0 Hz and 8.1 Hz, respectively.

The last two QPSO candidates are not persistent throughout the entire duration of their respective bursts. The QPSO candidate in burst MET 254302590.741 (QPSOd) has a broader peak, with a peak frequency of 60.6 Hz and an FWHM of 17.02 Hz (WWZ),

Table 1
QPSO Candidates Using WWZ and LSP Methods

Name	MET	Begin Time (s)	End Time (s)	E_{piv}[a] (keV)	Initial E_{peak} (keV)	Final E_{peak} (keV)	WWZ (Top), LSP (Bottom)				p-value
							Peak Frequency (Hz)	HWHM (Hz)	Coherence (Q)	Cycle Count	
QPSOa	254366383.448	–0.01[b]	0.11[b]	29	$35.14^{+1.08}_{-1.02}$	$30.52^{+0.75}_{-0.73}$	28.97(8)	3.55(4)	4.09	3.48	0.0568
							27.90(1)	5.43(5)	2.57	3.35	0.0066
QPSOb	254299756.841	–0.03	0.26	15	$20.58^{+0.82}_{-0.90}$	$12.98^{+1.27}_{-1.55}$	15.73(4)	1.33(5)	5.89	4.56	0.0001
							…	…	…	…	…
QPSOc	254291434.732	0.0[b]	0.15[b]	15	$40.32^{+1.25}_{-1.15}$	$40.32^{+1.25}_{-1.15}$	27.79(4)	4.02(1)	3.46	4.17	0.1021
							29.45(2)	4.07(7)	3.62	4.42	0.012
QPSOd	254302590.741	0.04	0.08	29	$35.78^{+1.02}_{-0.97}$	$35.78^{+1.02}_{-0.97}$	60.56(1)	8.51(1)	3.56	2.42	0.1163
							67.84(4)	12.29(18)	2.76	2.71	0.1249
QPSOe	254279323.706	0.19	0.29	18	$34.74^{+1.74}_{-1.51}$	$41.90^{+1.28}_{-1.14}$	37.13(1)	4.86(3)	3.82	3.71	0.1258
							35.50(3)	7.42(12)	2.39	3.55	0.0026

Notes.
[a] E_{piv} represents the pivot energy of the HR.
[b] The QPSO candidate persists throughout the entire burst.

and 67.8 Hz with an FWHM of 24.6 Hz (LSP). The QPSO duration is only 0.04 s, considerably shorter compared to other candidates, whose durations are on the order of 0.10 s. Therefore, it has a slightly higher p-value of around 0.12. On the other hand, the candidate in burst MET 254279323.706 (QPSOe) has peak and FWHM values of 37.13 and 9.71 Hz (using WWZ) and 35.5 and 14.8 Hz (using LSP). Finally, their corresponding p-values are 0.1258 and 0.0026, respectively.

5. Discussion

SGR J1550−5418 burst spectra have been investigated both in a time-integrated and time-resolved manner in the past. G. Younes et al. (2014) performed time-resolved spectral analysis of 63 bursts of SGR J1550−5418. Note that 40 out of our sample of 44 events are also included in their sample of 63 bursts. However, there are key methodological differences between our study and theirs. G. Younes et al. (2014) extracted spectra using much finer time resolution, with time bins defined based on the signal-to-noise ratio. In contrast, our study segments bursts based on spectral similarity with clustering to identify natural change points in spectral evolution. Let us first compare our results to theirs. Using the COMPT model, they found a Gaussian distribution for the photon index with a mean of −0.55, which is compatible with our result. In addition, they found broken-power-law relationships between flux and the two parameters of the COMPT model with a break around $f \sim 10^{-5}$ erg cm^{-2} s^{-1}.

We find a similar broken-power-law relation between flux and E_{peak} with slopes -0.10 ± 0.07, 0.12 ± 0.04 and a break point at $(6.17 \pm 2.41) \times 10^{-6}$ erg cm^{-2} s^{-1}. These values are consistent with their results within the uncertainties. However, we also find that this relation can be modeled by a single power law with a comparable BIC value ($\Delta\mathrm{BIC} \approx 1$ between the single and broken-power-law models) with a power-law index of 0.04 ± 0.02 (left panel of Figure 7). This is likely due to the limited sample size and narrower flux range compared to the data set of G. Younes et al. (2014). To further test whether our current data set is sufficient to robustly detect a break (if one truly exists), we performed a jackknife resampling analysis (J. W. Tukey 1958). We find that the estimated break point in the E_{peak}–flux relation is highly stable, with a standard deviation of only 0.03 dex, which suggests the break point location is not overly sensitive to individual data points. As for the photon index versus flux plot, they reported no correlation up to the break point of $\sim 10^{-5}$ erg cm^{-2} s^{-1}, then a similar positive correlation as in E_{peak} versus flux. We find that the flux–photon index relation can also be described by a single power law as well as a broken power law. However, the jackknife analysis reveals that the break point estimate is unstable, with a standard deviation of 0.21 dex. Moreover, when employing a broken power law, only two data points remain on the high-flux side of the break point. Therefore, we adopt a single power-law model with a slope of 0.72 ± 0.06 for the entire flux range (see right panel of Figure 7).

G. Younes et al. (2014) also investigated the relationship between the blackbody temperature (kT) and the surface area of the inferred emission region (R^2) in four flux regimes. They showed that the R^2 versus kT values follow a broken-power-law trend for the two parameters above $10^{-4.5}$ erg cm^{-2} s^{-1}; for flux below this, the trend is consistent with a single power law. We find a similar broken-power-law trend at the highest flux levels ($F > 10^{-4.5}$ erg cm^{-2} s^{-1}) and a single power-law trend can describe R^2 versus kT in all lower-flux regimes (see Figure 8).

We also investigated the R^2 versus kT behavior using the parameters of the MBB-RCS model with the same flux intervals (see the right panel of Figure 8). The MBB-RCS model was not used in G. Younes et al. (2014). We find that they are all well represented by single power laws (see Table 2 for power-law indices). We find that in all flux regimes the trends are consistent with the expectations of the Stefan–Boltzmann law ($R^2 \propto kT^{-4}$), except for a slight deviation in the highest-flux regime.

We compared the results of the SGR J1550−5418 investigations with those of Ö. Keskin et al. (2024), who employed the same spectral analysis approach for the bursts of SGR J1935+2154. In the analysis of the COMPT model, there are notable differences in the flux relationships of both parameters. In SGR J1935+2154, both parameters and flux values have a broken-power-law relation. The correlation

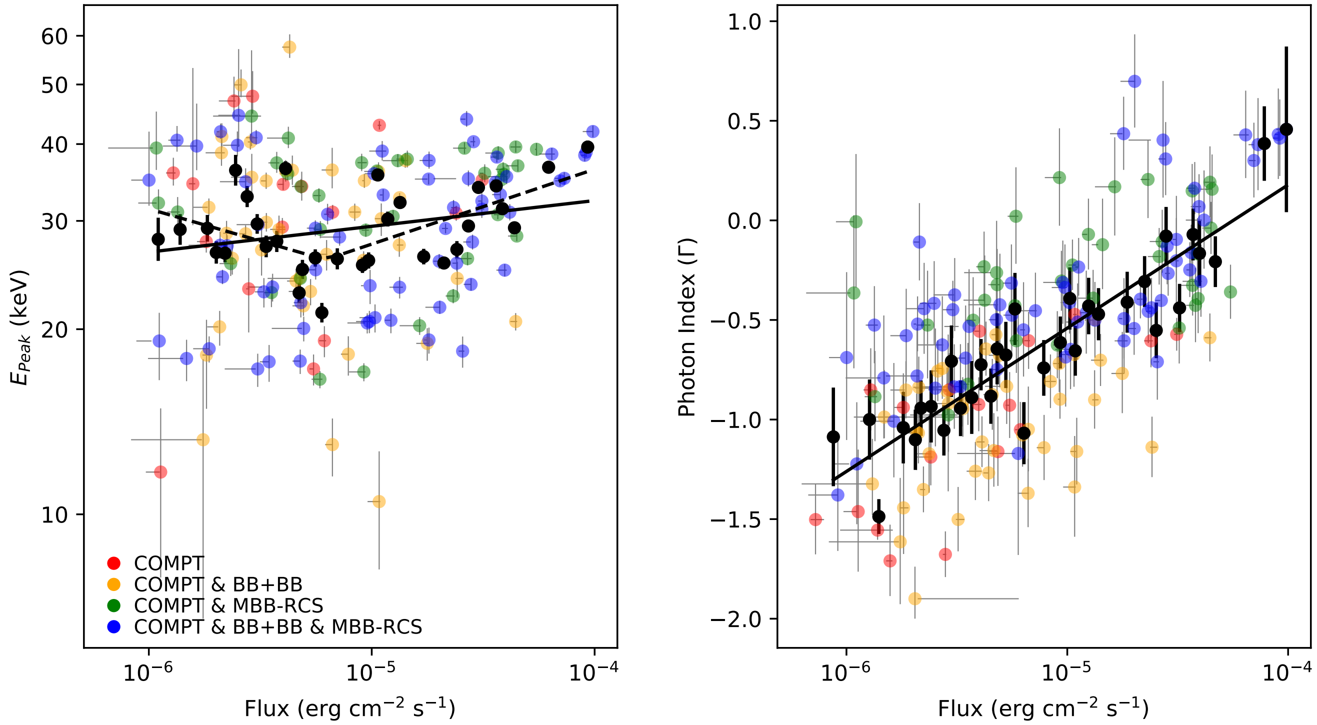

Figure 7. Scatter plot of COMPT $E_{\rm peak}$ vs. flux (left panel) and photon index vs. flux (right panel). Color-coding shows the preferred photon model(s) based on BIC values. The black dots represent the weighted means of consecutive groups, each with 10 data points. The black lines show the best single power-law fit to the relation between the weighted means of $E_{\rm peak}$ and flux, and between the weighted means of photon index and flux, respectively. The dashed line shows the best broken-power-law fit between the weighted means of $E_{\rm peak}$ and flux.

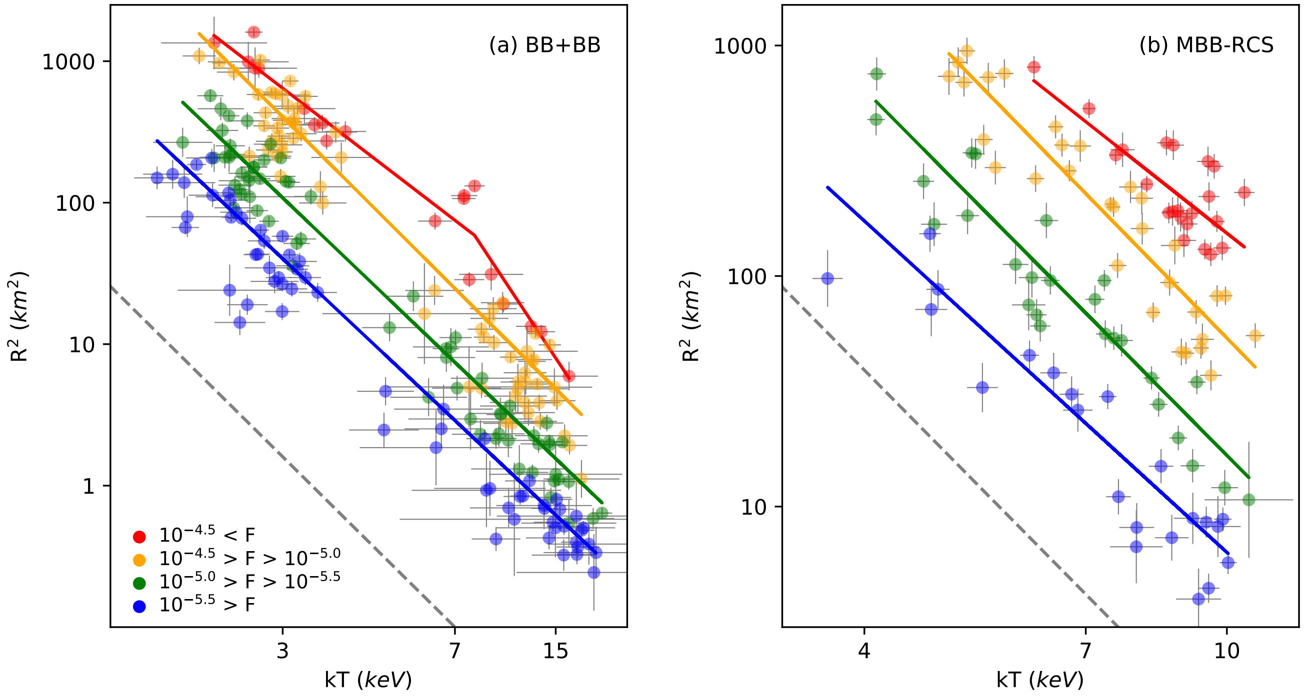

Figure 8. Left panel: flux color-coded plot of R^2 vs. kT for BB+BB. Each data point represents the weighted means of R^2 and kT of every two time segments only for display purposes. Solid lines show the best-fit models. Right panel: flux color-coded scatter plot of R^2 vs. kT for MBB-RCS. Solid lines represent power-law fits. We take the source distance as 5 kpc. In both panels the gray dashed line represents $R^2 \propto T^{-4}$.

between $E_{\rm peak}$ and flux is positive, which becomes steeper after a break value. Similarly, the photon index initially shows a positive correlation with flux but transitions to a negative correlation beyond the break. Conversely, in SGR J1550 −5418, the flux–$E_{\rm peak}$ relationship can be explained with either a slight positive correlation or a broken-power-law relation as described above. Thus, the flux–photon index has a strong positive correlation, with $\alpha = 0.72 \pm 0.06$.

In the analysis of the BB+BB model, there is a distinct positive correlation between kT_l and kT_h in both sources.

Table 2

Fit Results of the Trends between the Blackbody Emitting Area (R^2) vs. Temperature (kT) from the MBB-RCS and BB+BB Models

Flux Range (erg cm^{-2} s^{-1})	MBB-RCS α-kT_m	BB+BB α-kT_l	α-kT_h	kT_{break} (keV)
$F > 10^{-4.5}$	-3.12 ± 0.5	-3.10 ± 0.30	-6.12 ± 1.26	10.72 ± 1.12
$10^{-5.0} < F < 10^{-4.5}$	-4.04 ± 0.30	-4.03 ± 0.11[a]	…	…
$10^{-5.5} < F < 10^{-5.0}$	-3.99 ± 0.30	-3.86 ± 0.08[a]	…	…
$F < 10^{-5.5}$	-3.61 ± 0.31	-3.80 ± 0.06[a]	…	…

Note.

[a] A single power-law fit to the data.

Second, flux and both kT values have a positive correlation in SGR J1935+2154. In contrast, the highest flux values are accumulated around the peak of the Gaussian distribution in both kT_l and kT_h parameters of SGR J1550−5418. Lastly, the relationship between R^2 and kT values in the BB+BB model can be fit with a broken power law for SGR J1935+2154, except for the lowest-flux group, which can be fit with a single and a broken power law. On the other hand, SGR J1550−5418 parameters show single power-law fit characteristics, with the exception only of the highest-flux group, which shows a broken-power-law relation.

The MBB-RCS model fit results show similar characteristics for the bursts of the two magnetars. Namely, R^2 versus kT_m relations exhibit single power laws in all flux groups of both sources. It is worth mentioning that there is a significant deviation from the Stefan–Boltzmann law at the highest flux values in SGR J1935+2154. This deviation is expected since the MBB-RCS model (S. Yamasaki et al. 2020) assumes photons emitted from the fireball to scatter once by the magnetospheric particles in the resonant layer. This generates a tail in the spectrum at higher energies, and therefore a deviation from the Stefan–Boltzmann law. However, even at the highest flux levels ($F > 10^{-4.5}$) in SGR J1550−5418, the slope value remains close to the expected value of –4 with $\alpha = -3.12 \pm 0.5$. This suggests that a single-scattering case is sufficient to account for the observed burst spectra of SGR J1550−5418, in contrast to the deviations seen in SGR J1935+2154.

In the framework proposed by the MBB-RCS model fit results for SGR J1935+2154 (Ö. Keskin et al. 2024), such deviations from the Stefan–Boltzmann law were interpreted as signatures of anisotropic radiation fields near the apex of an extended magnetic flux tube. In this picture, the highly optically thick plasma in the emission region cools adiabatically as it flows from smaller, hotter regions near the flux tube footpoints on the stellar surface to the larger, cooler regions near the equatorial apex. This geometry results in the observed spectral extension. If the deviation from the canonical R^2–kT^4 relation seen in SGR J1935+2154 indeed reflects the spatial extent and geometry of the active emission region—modeled as a broad, flaring flux tube—then the absence of such a deviation in SGR J1550−5418 may instead reflect differences in tube structure or the strength of radiative anisotropy.

Specifically, the tube length can be estimated as $R_l \sim 4R^2/R_t$, where R_t is the transverse cross section of the flux tube at its apex. Although the observed values of R^2 in SGR J1550−5418 are higher (up to $\sim$1000 km^2) than those in SGR J1935+2154 (a few hundred square kilometers; Ö. Keskin et al. 2024), this may correspond to a proportionally larger cross section of the apex R_t, resulting in a thicker, more compact flux tube. In such a geometry, the anisotropy of the emergent radiation—arising from direction-dependent Compton scattering in low-magnetic-field regions—is likely reduced. Consequently, the observed radiation remains more isotropic, preserving the expected Stefan–Boltzmann slope even at high altitudes where anisotropic effects would otherwise dominate.

As far as the oscillation characteristics of QPSO candidates obtained (see Table 1), QPSOa and QPSOc (and possibly QPSOe as well) exhibit very similar oscillation frequencies of around 28 Hz. Therefore, there are two (or possibly three) bursts with a QPSO frequency of near 30 Hz, one very bright and long burst with a QPSO frequency of around 15 Hz, and another burst with a shorter QPSO at approximately 60 Hz. These frequencies hint at a potential harmonic pattern, suggesting that 28 Hz may lie near the fundamental frequency, making the 15 Hz signal its subharmonic and 60 Hz its first harmonic.

Regarding the evolution of E_{peak} during the QPSO candidates, all except one (QPSOb) have E_{peak} values between 30 and 40 keV, which coincide with the mean and the denser central region of the parameter distribution (see Figure 3). No E_{peak} evolution is observed in QPSOc and QPSOd since both occur within a single time segment. In QPSOa, the parameter decreases from approximately 35 to 30 keV, whereas in QPSOe, it increases from 35 to around 42 keV. However, since each of these four bursts consists of at most three time segments, drawing definitive conclusions about the temporal evolution of E_{peak} is difficult. Conversely, the photon index parameter stays constant within its 1σ error range throughout the time segments.

On the other hand, QPSOb (Figure 6(b)) spans over eight of the total of nine time segments. During this period, E_{peak} starts at approximately 20 keV, follows a two-peaked trend similar to the light curve, reaching 22–23 keV at both peaks before decreasing to around 13 keV. Between the beginning and the end of this two-peaked behavior, there is approximately 0.17 s, which is slightly more than twice the QPSO candidate period ($\sim$0.07 s). This suggests that the observed spectral modulation follows a periodic trend with each peak aligning with a cycle of the QPSO. The slight deviation from an exact integer multiple may indicate variations in the oscillation over time.

The second parameter of the COMPT model, the photon index, shows a subtle evolution in QPSO candidates with more than one time segment (QPSOs a, b, and e). During QPSOs a and b, the photon index parameter slightly decreases from 0.40 to −0.07 and −0.34 to −1.05, respectively. A similar two-peaked behavior is also present in the photon index of QPSOb, though it is less distinct compared to E_{peak}.

The theoretical interpretation of QPSOs likely differs from standard QPO models, which are typically attributed to torsional shear oscillations in the magnetar's crust triggered by its twisted magnetosphere. O. J. Roberts et al. (2023) propose a novel model for QPSOs in magnetars, attributing them to density and pressure perturbations within a highly magnetized flux tube. According to this model, Thomson scattering should be dominant since the burst emission zone is highly optically thick due to high densities of radiating charges. Consequently, since Alfvén waves would be absorbed and dispersed in the dense plasma, it is unlikely that they are the cause of the observed E_{peak} oscillations. The proposed mechanism involves variations in density and pressure moving along a magnetized flux tube. These fluctuations cause adiabatic compression and expansion, which leads to variations in E_{peak}.

We applied the prescription explained in O. J. Roberts et al. (2023) as follows: E_{peak} values of QPSO candidates are measured in the range of 30–40 keV (with the exception of QPSOb; see Table 1), which implies a plasma temperature of approximately $kT \sim 10$ keV. This corresponds to $\Theta = kT/m_e c^2 \approx 0.02$, which leads to a sound speed that aligns with the classical nonrelativistic estimate of $c_s^2/c^2 \approx 5\Theta/3$ (assuming an adiabatic index $\gamma = 5/3$). Therefore, the 3D sound speed is calculated as $c_s \approx 0.176c$. Finally, the time required for the pair plasma to propagate over the neutron star is $R_{\text{NS}}/c_s \sim 0.18$ ms as presented in O. J. Roberts et al. (2023). Assuming $R_{\text{NS}} = 10^6$ cm, a fluctuation of 35 ms (≈28 Hz; QPSOs a, c, and e) corresponds to acoustic wave propagation along a flux tube with an approximate length of $\mathcal{S} \sim 190 R_{\text{NS}}$. If the fluctuation is around 16 ms (≈60 Hz; QPSOd), the length of the flux tube becomes $\mathcal{S} \sim 90 R_{\text{NS}}$. However, these lengths could be shorter due to adiabatic cooling along the flux tube. For QPSOb, E_{peak} evolves approximately from 20 to 13 keV, which corresponds to $kT \sim 5$ keV. After repeating all calculations for this kT value, for a fluctuation of around 67 ms (≈15 Hz) we obtain a flux tube length of $\mathcal{S} \sim 260 R_{\text{NS}}$. In this scheme, $\mathcal{S}$ ranges from about 100 to $250 R_{\text{NS}}$ with our results. It is important to note that QSPOs are a new phenomenon, and the sample investigated as well as oscillations found here are indicative but too limited to conclude as to any universal behavior.

Acknowledgments

We thank the anonymous reviewer for valuable comments and recommendations, which improved the quality and clarity of our manuscript. M.D., E.G., Y.K., and Ö.K. acknowledge support from the Scientific and Technological Research Council of Turkey (TÜBİTAK) through grant No. 121F266. S.Y. acknowledges the support from NSTC through grant Nos. 113-2112-M-005-007-MY3 and 113-2811-M-005-006.

Appendix

A list of all bursts used in this study is given in Table A1.

Table A1
Table of SGR J1550−5418 Bursts Used in This Study

Burst Date (yymmdd)	UTC	MET[a] (s)	Duration[b] (s)	No. of Overlapping Time Segments	No. of Nonoverlapping Time Segments	QPSO Candidates
090122	00:56:35.317	254278597.317[c]	0.517	3	1	…
090122	00:57:20.410	254278642.410	0.656	7	2	…
090122	00:58:00.842	254278682.842[c]	0.524	2	…	…
090122	01:08:41.706	254279323.706	0.915	10	3	QPSOe
090122	01:14:45.985	254279687.985	0.300	8	2	…
090122	01:16:28.686	254279790.686[c]	0.280	4	1	…
090122	01:18:10.302	254279892.302[c]	0.336	3	1	…
090122	01:18:42.351	254279924.351[c,d]	0.248	1	…	…
090122	01:25:18.640	254280320.640	0.540	5	2	…
090122	01:28:59.988	254280541.988[d]	0.516	4	2	…
090122	02:32:53.944	254284375.944	0.296	4	2	…
090122	02:54:00.999	254285642.999[c,d]	0.698	1	…	…
090122	04:09:08.677	254290150.677	0.808	7	2	…
090122	04:12:33.001	254290355.001	0.849	6	2	…
090122	04:30:32.732	254291434.732[c]	0.433	4	1	QPSOc
090122	04:32:19.025	254291541.025[c]	0.814	3	1	…
090122	04:32:49.462	254291571.462[d]	0.687	12	5	…
090122	04:33:28.047	254291610.047[c]	0.192	2	…	…
090122	04:34:09.362	254291651.362[d]	0.954	19	6	…
090122	04:34:18.108	254291660.108[c]	0.484	3	1	…
090122	04:34:20.687	254291662.687	1.187	10	2	…
090122	04:40:06.444	254292008.444[c]	0.491	2	…	…
090122	04:40:28.785	254292030.785[c]	0.464	1	…	…
090122	05:14:03.372	254294045.372[d]	1.048	11	5	…
090122	05:14:29.229	254294071.229	0.891	10	3	…
090122	05:16:06.849	254294168.849	0.153	9	3	…
090122	05:16:18.303	254294180.303[c]	0.616	2	…	…
090122	05:16:44.241	254294206.241[c]	0.215	5	1	…
090122	05:52:15.165	254296337.165[c,d]	0.560	2	…	…
090122	06:03:35.989	254297017.989	0.448	14	4	…
090122	06:49:08.655	254299750.655	0.751	18	4	…

Table A1
(Continued)

Burst Date (yymmdd)	UTC	MET[a] (s)	Duration[b] (s)	No. of Overlapping Time Segments	No. of Nonoverlapping Time Segments	QPSO Candidates
090122	06:49:14.841	254299756.841	1.364	26	8	QPSOb
090122	06:49:32.952	254299774.952	0.548	10	3	…
090122	06:49:44.192	254299786.192	0.609	8	2	…
090122	06:49:48.471	254299790.471[d]	0.939	8	8	…
090122	06:50:08.622	254299810.622[d]	0.390	12	3	…
090122	06:50:12.076	254299814.076	0.419	7	2	…
090122	06:50:14.271	254299816.271[c]	0.281	6	1	…
090122	06:50:22.533	254299824.533[c]	1.291	3	1	…
090122	06:50:49.339	254299851.339[d]	0.622	3	2	…
090122	06:50:50.911	254299852.911[c]	1.844	2	…	…
090122	06:50:57.268	254299859.268[c,d]	0.405	2	…	…
090122	06:51:08.154	254299870.154[c]	0.601	2	…	…
090122	06:51:14.791	254299876.791[d]	1.165	31	9	…
090122	06:52:00.167	254299922.167[d]	0.264	6	3	…
090122	06:52:03.979	254299925.979	0.678	12	4	…
090122	06:52:20.032	254299942.032[c]	0.577	3	1	…
090122	06:59:35.546	254300377.546[d]	1.080	6	2	…
090122	07:00:58.715	254300460.715[d]	0.665	11	4	…
090122	07:26:29.656	254301991.656	0.917	10	2	…
090122	07:31:14.748	254302276.748[d]	1.420	21	5	…
090122	07:36:28.741	254302590.741[c]	0.464	3	1	QPSOd
090122	07:40:15.939	254302817.939[d]	0.602	9	3	…
090122	08:36:30.674	254306192.674[d]	1.152	3	2	…
090122	10:03:04.670	254311386.670[d]	0.429	6	3	…
090122	10:16:40.374	254312202.374[c]	0.387	4	1	…
090122	12:00:48.740	254318450.740[c]	0.565	6	1	…
090122	15:02:15.402	254329337.402[c,d]	0.236	2	…	…
090122	15:35:53.655	254331355.655[d]	0.208	5	2	…
090122	23:14:54.053	254358896.053[d]	0.520	16	6	…
090122	23:31:19.876	254359881.876	0.428	4	2	…
090123	01:19:42.448	254366383.448	0.144	8	3	QPSOa
090123	02:42:10.695	254371330.695[d]	0.592	17	5	…
090123	16:54:38.064	254422479.064	0.220	6	3	…
090125	12:55:21.265	254580923.265[c]	0.072	1	…	…
090125	23:00:36.087	254617238.087[d]	0.980	9	3	…
090203	20:00:39.494	255384041.494	0.272	16	5	…
090204	20:27:20.796	255472042.796[d]	0.236	5	3	…
090214	19:31:45.276	256332707.276[c,d]	0.188	1	…	…
090221	15:27:34.404	256922856.404[c,d]	0.228	2	…	…
090222	21:44:49.908	257031891.908[c,d]	0.108	1	…	…
090223	03:04:40.789	257051082.789[c,d]	0.152	4	1	…
090322	22:39:15.786	259454357.786[d]	0.592	9	3	…
090401	15:59:36.826	260294378.826	0.208	4	2	…

Notes.
[a] Mission Elapsed Time, the number of seconds since 2001 January 1.
[b] Duration of the Bayesian block.
[c] Bursts with only one or none (…) nonoverlapping time segments are not presented in the results.
[d] Saturated burst.

ORCID iDs

Mustafa Demirer https://orcid.org/0009-0000-9126-7824
Ersin Göğüş https://orcid.org/0000-0002-5274-6790
Yuki Kaneko https://orcid.org/0000-0002-1861-5703
Özge Keskin https://orcid.org/0000-0001-9711-4343
Sinem Şaşmaz https://orcid.org/0000-0002-9669-5825
Shotaro Yamasaki https://orcid.org/0000-0002-1688-8708

References

Astropy Collaboration, Price-Whelan, A. M., Lim, P. L., et al. 2022, ApJ, 935, 167
Atteia, J. L., Boer, M., Hurley, K., et al. 1987, ApJL, 320, L105
Atwood, W. B., Abdo, A. A., Ackermann, M., et al. 2009, ApJ, 697, 1071
Baluev, R. V. 2008, MNRAS, 385, 1279
Bochenek, C. D., Ravi, V., Belov, K. V., et al. 2020, Natur, 587, 59
Camilo, F., Ransom, S. M., Halpern, J. P., & Reynolds, J. 2007, ApJ, 666, L93

Cash, W. 1979, ApJ, 228, 939
Collazzi, A. C., Kouveliotou, C., Horst, A. J., et al. 2015, ApJS, 218, 11
Duncan, R. C. 1998, ApJL, 498, L45
Duncan, R. C., & Thompson, C. 1992, ApJL, 392, L9
Feroci, M., Caliandro, G. A., Massaro, E., Mereghetti, S., & Woods, P. M. 2004, ApJ, 612, 408
Foster, G. 1996, AJ, 112, 1709
Huppenkothen, D., D'Angelo, C., Watts, A. L., et al. 2014, ApJ, 787, 128
Huppenkothen, D., Watts, A. L., Uttley, P., et al. 2013, ApJ, 768, 87
Hurley, K., Cline, T., Mazets, E., et al. 1999, Natur, 397, 41
Israel, G. L., Belloni, T., Stella, L., et al. 2005, ApJL, 628, L53
Israel, G. L., Romano, P., Mangano, V., et al. 2008, ApJ, 685, 1114
Kaastra, J. S. 2017, A&A, 605, A51
Kaneko, Y., Göğüş, E., Kouveliotou, C., et al. 2010, ApJ, 710, 1335
Kass, R. E., & Raftery, A. E. 1995, JASA, 90, 773
Keskin, Ö., Göğüş, E., Kaneko, Y., et al. 2024, ApJ, 965, 130
Kırmızıbayrak, D., Şaşmaz Muş, S., Kaneko, Y., & Göğüş, E. 2017, ApJS, 232, 17
Lamb, R. C., & Markert, T. H. 1981, ApJ, 244, 94
Laros, J. G., Fenimore, E. E., Klebesadel, R. W., et al. 1987, ApJ, 320, L111
Li, X., Ge, M., Lin, L., et al. 2022, ApJ, 931, 56
Lin, L., Göğüş, E., Baring, M. G., et al. 2012, ApJ, 756, 54
Lin, L., Kouveliotou, C., Baring, M. G., et al. 2011, ApJ, 739, 87
Lomb, N. R. 1976, Ap&SS, 39, 447
Lyubarsky, Y. E. 2002, MNRAS, 332, 199
Lyutikov, M. 2003, MNRAS, 346, 540
MacQueen, J. B. 1967, in Proc. 5th Berkeley Symp. on Mathematical Statistics and Probability, Vol. 1, ed. L. M. L. Cam & J. Neyman (Berkeley, CA: Univ. California Press), 281
Mazets, E. P., Golenetskii, S. V., Ilinskii, V. N., Aptekar, R. L., & Guryan, Y. A. 1979, Natur, 282, 587
Meegan, C., Lichti, G., Bhat, P. N., et al. 2009, ApJ, 702, 791
Mereghetti, S., Götz, D., Weidenspointner, G., et al. 2009, ApJL, 696, L74
Palmer, D. M., Barthelmy, S., Gehrels, N., et al. 2005, Natur, 434, 1107
Pedregosa, F., Varoquaux, G., Gramfort, A., et al. 2011, JMLR, 12, 2825
Roberts, O. J., Baring, M. G., Huppenkothen, D., et al. 2023, ApJL, 956, L27
Scargle, J. D. 1982, ApJ, 263, 835
Scargle, J. D., Norris, J. P., Jackson, B., & Chiang, J. 2013, ApJ, 764, 167
Schwarz, G. 1978, AnSta, 6, 461
Strohmayer, T. E., & Watts, A. L. 2005, ApJL, 632, L111
Strohmayer, T. E., & Watts, A. L. 2006, ApJ, 653, 593
Thompson, C., & Duncan, R. C. 1995, MNRAS, 275, 255
Torrence, C., & Compo, G. P. 1998, BAMS, 79, 61
Tukey, J. W. 1958, Ann. Math. Stat., 29, 614
van der Horst, A. J., Kouveliotou, C., Gorgone, N. M., et al. 2012, ApJ, 749, 122
van der Klis, M. 2006, in Compact Stellar X-ray Sources, ed. W. H. G. Lewin & M. van der Klis, Vol. 39 (Cambridge: Cambridge Univ. Press), 39
von Kienlin, A., Gruber, D., Kouveliotou, C., et al. 2012, ApJ, 755, 150
Xiao, S., Li, X.-B., Xue, W.-C., et al. 2024, MNRAS, 527, 11915
Yamasaki, S., Lyubarsky, Y., Granot, J., & Göğüş, E. 2020, MNRAS, 498, 484
Younes, G., Kouveliotou, C., van der Horst, A. J., et al. 2014, ApJ, 785, 52